Millimeter-Wave Doppler Spectrum and Polarimetric Response of Walking Bodies

Mehrnoosh Vahidpour, *Student Member, IEEE*, and Kamal Sarabandi, *Fellow, IEEE*

Abstract—In this paper, the Doppler spectra of the radar backscatter response of human body and a quadruped are presented at W-band frequencies. This study is motivated by the desire to utilize millimeter-wave radars to detect pedestrians against other targets in the radar scene. The approach is based on dissecting the radar backscatter to isolate the radar returns from different body parts. The forward model is based on an iterative physical optics approach. The complex motion of different parts of walking bodies and their amplitude and range of motion is directly reflected in their radar cross section (RCS) and Doppler spectrum bandwidth. It is shown that the Doppler spectra and RCS differences are sufficient to distinguish a walking human from stationary and other moving objects. Radar polarimetry in conjunction with time-frequency analysis is examined as a method for detecting concealed carried objects. The overall backscatter is decomposed into components associated with the limbs and torso which are then utilized to enhance target detection.

Index Terms—Doppler effect, radar cross section (RCS), radar polarimetry.

I. INTRODUCTION

MILLIMETER-WAVE (MMW) radars are envisioned for a number of safety and security applications such as collision warning for vehicles, autonomous vehicle control, perimeter security, and detection of concealed weapons and explosives carried by individuals. Detection and identification of pedestrians in highly cluttered radar scenes, such as urban and highway environments, are also of great importance.

The MMW region of electromagnetic spectrum offers certain unique features that can be utilized in detection and identification of individuals from their surroundings. In this region, the wavelength is short enough to allow fabrication of compact size radars and achieve higher resolution. Yet, at the same time, the wavelength is long enough to allow signal penetration through nonconductive objects, clothing, smoke, and fog with little or no attenuation. Furthermore, MMW signals unlike X-rays are nonionizing, leading to minimal health risks. These make MMW band ideally suited for surveillance of individuals for many applications ranging from the identification of the human body itself to the detection of concealed weapons [1], [2]. As human bodies can be moving when they are under radar interrogation, such as in walking, jogging, or running,

their style of motion suggests some means of identification. Doppler radars are employed to capture the motion of the targets. Unlike optical and infrared measurements, the response of radar cannot be directly visualized and needs scanning and postprocessed. One way is using imaging radars [3]. Another way is investigating the radar signature from different angles or directions. In [4], a method is proposed to extract motion parameters from a radar measurement by minimizing the difference between the simulated model and real measurements. The Doppler signature cannot only be used to distinguish a human from the rest of the radar scene, but it can also be used to isolate the radar backscatter from different parts of the body. Feature extraction of body movements and human gait recognition based on Doppler radar has been investigated at lower microwave bands [5]–[9] qualitatively in which the human body is modeled by a uniform dielectric volume or unsophisticated models of homogeneous cylindrical and spherical objects. In [9], the features were extracted using the time-frequency transform of the response measured by a 24-GHz Doppler radar. The possibility to discriminate between human gait and those of other objects based on step rate and mean velocity was investigated as well.

The feasibility of detection of concealed objects carried on human body has also been investigated with different techniques. Traditional detection systems include metal detectors and X-ray systems. The latter has hazardous health effects when used on human, while the former can only be used in situ for detecting metallic objects [10]. More elaborate systems employ imaging techniques to identify the target and detect contraband [11]. These systems have been very effective, but have a number of shortcomings, such as requiring close proximity to the subject, slow processing, violating the privacy of individuals, and giving low-quality blurred images in a heavily cluttered environment. In [5], detection was investigated at low microwave frequencies, and slight decrease in the amplitude of the radar return is used to detect the presence of a rifle against a human body. However, for such techniques to be successful, the response of the human must be isolated from its surrounding, the radar needs to be radiometrically calibrated, and the radar cross section of the human subject at the proper aspect angle and posture without the rifle must be known. Considering the fact that the number of conditions one may encounter (different body and object sizes and shapes) is enormous, algorithms that rely on quantitative radar cross section (RCS) values cannot be very reliable. To circumvent these difficulties to some extent, the application of polarimetric radars is proposed for which narrow beams with footprints commensurate to human body can be generated. Also, using radar polarimetry, radiometric
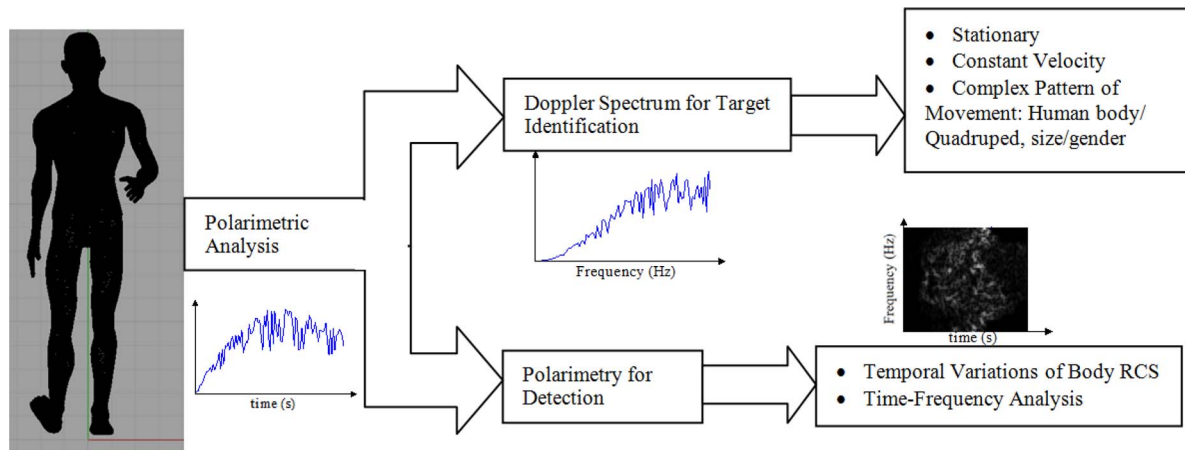
Fig. 1.   Procedures used for target discrimination and detection. The time domain polarimetric response of the walking body undergoes processes such as Fourier transform and time-frequency analysis to derive a means for identifying human body and detecting concealed objects.

calibration will not be required. However, at lower microwave frequencies, the human body can depolarize the backscatter signal considerably, and therefore cross-polarized signature cannot effectively be used. In addition, for narrow beamwidths, very large antennas are required. At high MMW frequencies, the amount of copolarized backscatter response is dominant for smooth targets, and cross-polarized response represents the level of smoothness and symmetry of the target. Uneven and asymmetric targets generate greater cross-polarized response. The geometries of common concealed objects carried by individuals are highly irregular and, once placed near human body, can indeed increase the level of cross-polarized backscatter observed by MMW radars. Therefore, at higher MMW frequencies, a significant increase in the cross-polarized response can be an indication of an external irregular object and can be used for detection.

In this paper, a polarimetric analysis of a walking human body and the associated Doppler spectrum are proposed for high MMW frequencies. A high-frequency technique based on iterative physical optics (PO) and geometric optics (GO) is used to generate both the co- and cross-polarized backscatter response of these targets at W-band. It is shown that the field scattered from a moving subject undergoes Doppler modulation of a particular signature as a result of the object motion. Hence, the unique features of motion and the radar backscatter contribution of different body parts are accurately captured by the Doppler spectrum and can be exploited for target identification. In order to investigate the feasibility of detecting external carried objects, time-frequency analysis is applied to the backscatter Doppler spectrum of a walking human to isolate the torso response where such objects are commonly concealed. This response is used to detect concealed objects. The presented detection algorithms does not require radar radiometric calibration, it relies only on the ratio of cross- to copolarized response of measured backscatter. As shown in Fig. 1, the time domain polarimetric response of the walking body is processed via the Fourier transform and time-frequency analysis to derive a means for identification and detection.

The paper is organized as follows. In Section II, the forward scattering model for predicting the backscatter response of

TABLE I

HUMAN SKIN DIELECTRIC CONSTANT PREDICTED BY ANALYTICAL MODELS AND MEASUREMENT. THE RESULTS SHOW THAT THE VALUE OF THE REFLECTION COEFFICIENT UNDERGOES ONLY MAXIMUM OF 6% DEVIATION. BY TAKING THE RATIO OF CROSS- TO COPOLARIZED RESPONSE, THE EFFECT OF THE DIELECTRIC CONSTANT IS EVEN LESS IMPORTANT

		Relative permittivity (95 GHz)	Loss tangent (95 GHz)	Reflection coefficient at normal incidence (magnitude)
Debye model [12]		6.11	1.42	0.4333
Four term Cole-Cole expression (Walters [13])		5.8	1.3	0.4218
Four term Cole-Cole expression (Gabriel [14])		7.51	1.156	0.4691
Measurement with open-ended waveguide	Sample 1	5.7	1.12	0.4163
	Sample 2	6	1.05	0.4254

human body at W-band frequencies is described. In Section III, methods for generating models of human bodies, dog, and a generic handgun models as well as their realistic motion models are presented. Section IV presents the Doppler spectrum analysis of the walking bodies. In Section V, the application of radar polarimetry and time-frequency analysis for detection of metallic and irregular objects against a human body is described.

II. MILLIMETER-WAVE SCATTERING MODEL

At W-band frequencies, dimensions of a typical human body are very large compared to the wavelength, and therefore methods based on full-wave analysis are not practical for present computers. However, the radii of curvature on human body are much larger than the wavelength which makes it a suitable candidate for high-frequency methods. The electric permittivity of the human skin at MMW frequencies can be calculated from a number of methods listed in Table I. In addition, we conducted a series of dielectric measurements using an open-ended waveguide attached to the frequency extenders of a

vector network analyzer. We found out even for a specific person, depending on the location, skin dielectric constant can change considerably. This variability depends on the moisture, skin thickness, etc. Table I shows some sample measurements showing this variability and a comparison with the proposed models. This table also shows the Fresnel reflection coefficient at normal incidence for each value of dielectric constant. This comparison is made to indicate that the surface reflectivity is not much affect by the small variations predicted by different models and the measured values. In addition, by taking the ratio of cross- to copolarized response, this effect is even less important.

Obviously, the dielectric constant predicted by all models and measurements is very lossy and highly reflective material with a very small skin depth. From the Debye model, it can be calculated as

$$\frac{\delta}{\lambda_0} = \frac{1}{\pi}\sqrt{\frac{1}{2\mathrm{Im}(\varepsilon_r)}} = 0.0763 \qquad (1)$$

which corresponds to 0.24 mm at 95 GHz. Thus a homogenous dielectric can be assumed, and the equivalent induced electric and magnetic currents on the surface of the body can be approximated using the PO model. In this approach, the scattered fields are approximated by the reflected fields from a local tangent planes of the object. The PO model for human body should perform well as the penetration depth is small, and as a result the multipath within the dielectric body can be ignored. However, the PO approach does not account for the interactions between different body parts and, therefore, does not guarantee the accuracy of the cross-polarized response. To account for the interactions and enhance the accuracy, the iterative PO (IPO) method is employed and utilized for human body analysis to calculate the total scattered field and the scattering matrix of the human target. The formulation of the approach is described in the Appendix.

It is worth mentioning here that most clothings appear mainly transparent at MMW frequencies. This fact is used nowadays in most prevalent MMW imaging systems installed at the airports. Even for thicker clothing where attenuation can be slightly higher than the usual, the clothing alone does not increase the ratio of cross- to copolarized ratio which the metric we use for detection of relatively large concealed objects.

III. MODELS AND METHODOLOGY

To calculate the polarimetric radar signature of moving bodies, we have been provided with the models of walking human bodies and dog by the University of Michigan 3-D Animation Laboratory. The initial humanoid models were created using reference photographs of real individuals to ensure proportions of the character were correct. Another set of the models were created by 3-D laser scans of human body. Then a digital model is created based on the proportions of the character to generate the human body shape. Specific to this project is an algorithm to attach a scanned body mesh to the skeletal structure. For this, it is required to assign each vertex/point of the mesh to the appropriate bone. In areas such as the shoulder or hips,
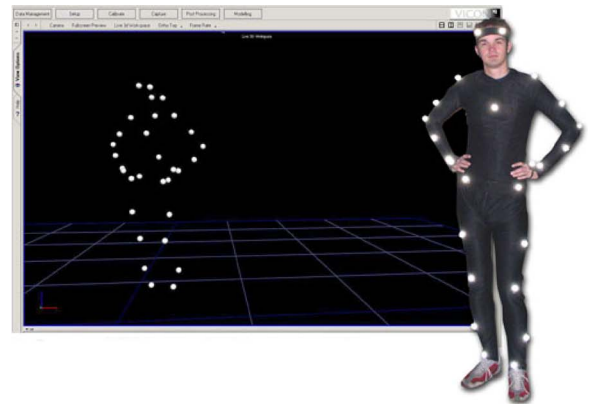
(a)
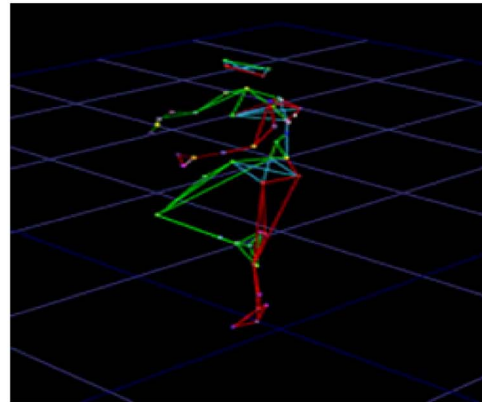
(b)

Fig. 2. (a) A person wears the lycra suit equipped with reflectors. The captured positions of these reflectors from one of the cameras are shown in the right inset. (b) The captured positions of the reflectors estimate a skeleton.
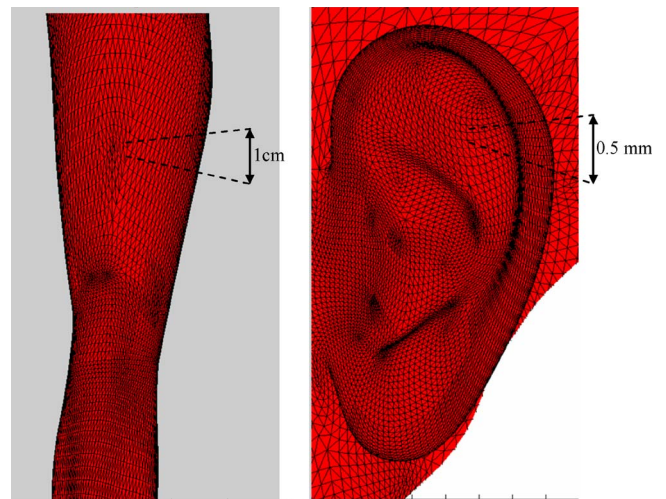

Fig. 3. Degree of discretization for various parts of body is presented. The facets are finer in areas like ear, while they are coarser in areas like thigh.

one specific point needs to receive influence from multiple bones to create a smooth deformed surface. 3-D models are ultimately comprised of many individual triangles which are placed side-by-side to construct a surface. These triangles were placed in strategic locations to generate the appearance of a human body. Once the mesh has been bound to the underlying skeleton, it is free to animate. The movements are replicated
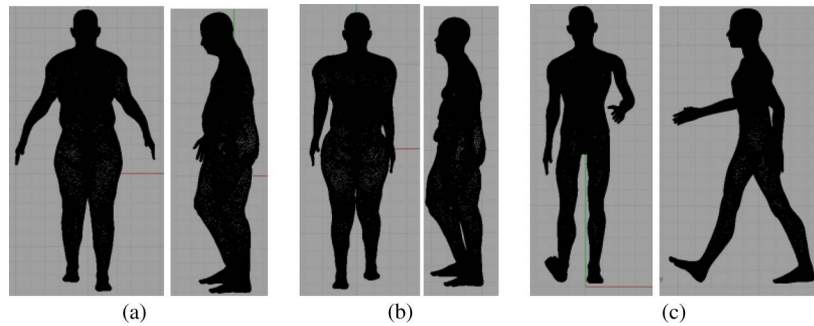
Fig. 4. Human bodies with different sizes and genders Front and side views are presented for (a) oversize male body (b) ovesize female body and (c) thin male body.
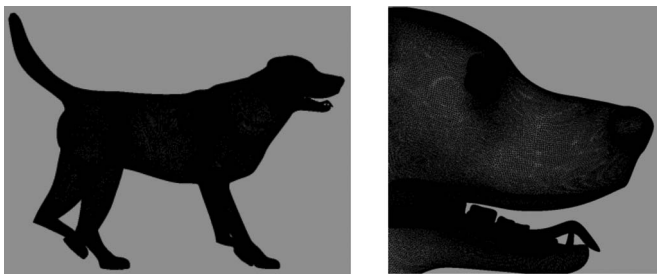

Fig. 5. Surface model of a dog. The surface of the body is discretized into triangular facets and all the facet's coordinates, and normal vectors are exported for analysis.
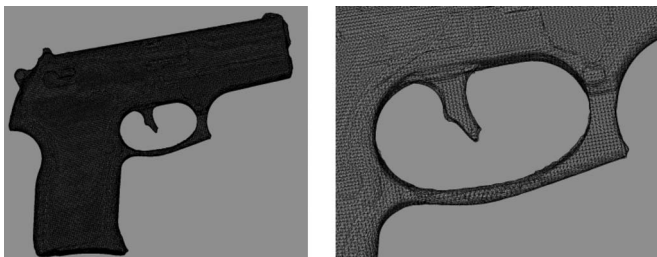

Fig. 6. Surface model of a generic handgun and the degree of discretization.

from captured video frames of a real person. In this motion capture system, the subject wears a lycra suit equipped with small, ball-shaped reflectors. An example of a human wearing such a suit is shown in Fig. 2(a). Each reflector ball is covered by a special retroreflective material and strategically placed on the subject. A set of eight cameras then track the reflectors as the subject moves. A computer communicates with each camera and cross references what the cameras "see" to calculate the position of each marker in space. Fig. 2(b) shows the skeleton reconstructed from the reflector points captured by one camera. For this project, the motion capture data were applied to the character and trimmed to a looping walk cycle that was 30 frames (∼1 s) in length. Having determined the body shape and gesture for each frame, a computer program discretizes the body surface into a number of triangular flat facets with nonuniform sizes provided that the areas are set to be below $\lambda/4$. The facet sizes are large in areas like the arms and legs, middle-sized in the torso, and very small in the hands, toes, and some facial parts. Fig. 3 shows the degree of discretization for various parts of body. Once the individual meshes representing

the various sections of the body were animated and set to the proper resolution, they were exported to the (stereolithography) STL format using a custom script written for 3-D Studio Max. The developed script analyzes the existing scene and exports the mesh at each time step. This file contains the coordinates of flat facets with nonuniform sizes on the surface of human body, along with their normal vectors. This technique is used to extract four walking human models: oversize and thin male and female bodies presented in Fig. 4.

A radar analysis of a walking dog is also considered and will be used to show the time-frequency response of a quadruped is different from that of a human being. A similar procedure is performed for a walking dog. In this analysis, a real dog (a short-haired Labrador) along with its anatomy is used as a reference to model and animate the walking dog. Thirty frames per second in one period of walking are measured and modeled. Then, the surface of the body in each frame is discretized to a number of triangular facets. As shown in Fig. 5, facets with dimensions below 0.5 mm can be located in the dog's face to take account of all the details.

As a part of the polarization analysis of irregular objects, a generic model of a handgun is also needed. For this purpose, 3-D laser scans of a handgun are taken. The data undergoes a similar process as above with the results shown in Fig. 6.

One important radar feature of walking bodies is their Doppler spectrum that can be utilized as a discriminator for a complex radar scene. The described models can be directly utilized to calculate the scattered field from which the Doppler spectra of walking bodies can be simulated directly by simulating a sequence of discrete body positions during a cycle of motion. However, the steps should be discretized into sufficiently small increments to satisfy the Nyquist rate for accurate computation of Doppler spectrum. For example, for a human subject walking at an average speed of 1.8 m/s, the distance between two successive frames (for 30 frames per second) is approximately 6 cm. This is much larger than the radar wavelength ($\lambda_0 \approx 3$ mm) and therefore, much finer increments are needed. To calculate the minimum number of required frames, the velocity of the fastest component of the body will be needed. Suppose the velocity of the fastest facet on the body, in radial direction from the radar, is represented by $v_{\max}$, then the resulting Doppler shift is $k_0 v_{\max}/\pi$. To satisfy the Nyquist rate, the sampling rate must satisfy $n \geq 4v_{\max}/\lambda_0$. For the example at hand, if the maximum velocity is assumed $v_{\max} = 5.5$ m/s, $n \geq 7000$, which clearly shows the initial
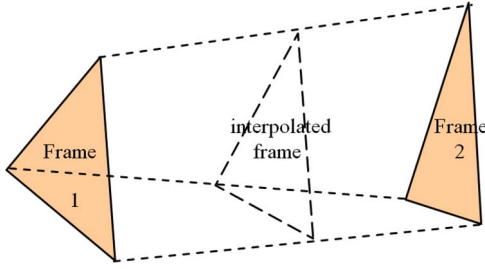
Fig. 7. Linear interpolation is performed between each two adjacent facets from each frame in order to estimate the "in-between" frames.

$n = 30$ frames are not sufficient. The process of exporting data for a larger number of frames is extremely time and memory consuming. To resolve this issue, since human motions are smooth, a linear interpolation scheme is used to create the intermediate frames between two key frames. For the human body example, if we can extract 250 frames between every two frames, a total number of 7500 frames is achieved which satisfies the Nyquist rate. The linear interpolation procedure is shown in Fig. 7 for two identical facets from two adjacent sequences. The coordinates of the vertices and the normal vectors for 248 facets in between is derived as

$$A_i = A_0 + i \frac{A_1 - A_0}{250} \qquad (2)$$

where $A_i = (x_i \ y_i \ z_i)$. Having determined the coordinates of all the facets of the 7500 frames, the backscattering response for each facet can be calculated using PO method and the total electric field of a frame by superposing all the responses: $\vec{E}_s = \sum_{n=1}^{N} \vec{E}_s^n$ where N is the number of facets. The scattering parameters for frames can then make a sequence as follows:

$$S_{xx} = \begin{pmatrix} S_{xx}^1 & S_{xx}^2 & \dots & S_{xx}^{7500} \end{pmatrix} \qquad (3)$$

where S_{xx}^i is the backscattering response of the xx component, of the ith frame. This sequence of the backscattering response generates a time domain signal which is Fourier transformed to derive the Doppler spectrum for each polarization.

IV. WALKING BODY ANALYSIS

A. Human Body

For PO simulation of the bodies, first GO is used to determine the shadowed and lit areas for a given orientation of the target with respect to the direction of the incident wave. To identify the lit facets, the $\hat{n} \cdot \hat{k}_i < 0$ condition, where $\hat{n}$ is the normal vector to the surface and $\hat{k}_i$ is the direction of incident wave is used. This condition alone is not sufficient to identify all shadow, and lit facets as in nonconvex surfaces some facets that satisfy the aforementioned condition can still be shadowed. This issue can be resolved easily using IPO solution as described before [17].

Fig. 8 shows the surface electric current distribution of the thin female subject (height $= 1.7$ m, weight $= 60$ Kg) illuminated by the radar beam at 95 GHz having a field intensity of 1 V/m from the front side (calculated from (11)—Appendix).
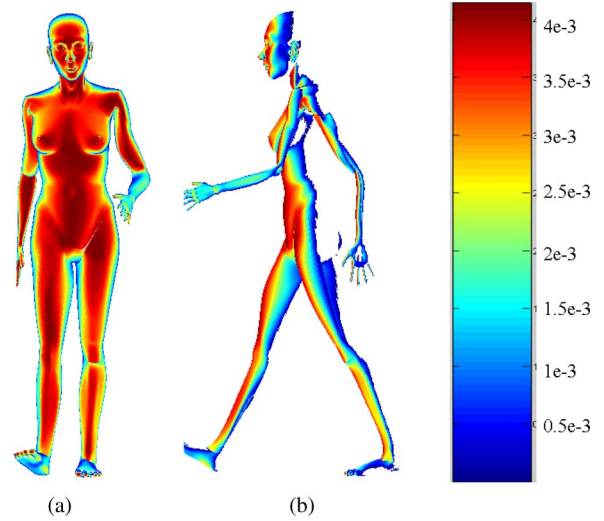

Fig. 8. PO surface electric current distribution on the surface of the thin female body with the incident field 1 V/m. (a) Front view. (b) Side view. Zero-induced currents on the backside is a result of the GO shadowing effect.
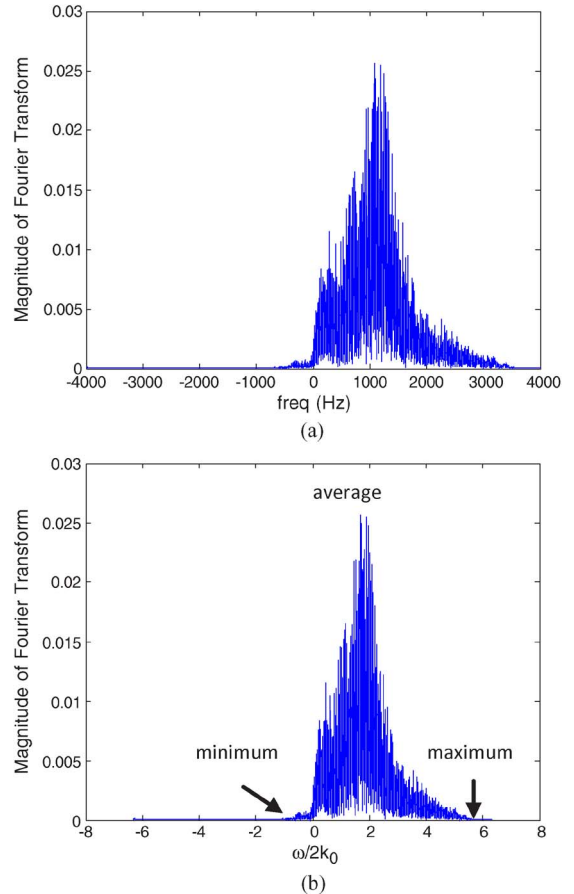

Fig. 9. Doppler spectrum of the copolarized radar response of the thin female body. (a) Versus frequency (95 GHz carrier removed). (b) Versus velocity $\omega_0/(2k_0)$. The range of velocity extends from -1 m/s to over $+5$ m/s. The average velocity which has the maximum amplitude is around $+1.8$ m/s and is actually the average velocity of walking. The maximum velocity found is about $+5.4$ m/s and is due to the feet.

As expected, there are no induced currents in the back part of the body, and near the shadow region, the surface currents diminish gently.
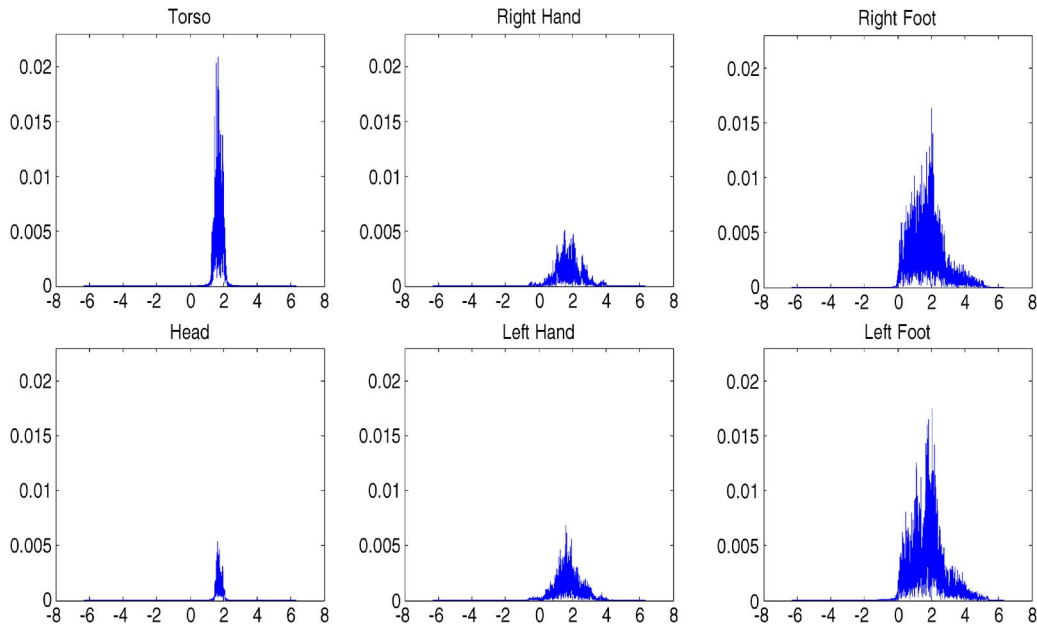
Fig. 10. Spectra of different body parts of the thin female model versus velocity are presented. The head and torso have similar spectra and bandwidth extends from 1.5 to 2.1 m/s around the average velocity of walking but the torso response has higher amplitude given its larger cross section. The legs and arms contain higher frequency content and hence higher velocities, as expected from their movement. The hands' spectra extend from −1 to 4 m/s with smaller amplitude while the spectra of the feet extend from 0 to 5.4 m/s with larger amplitude.
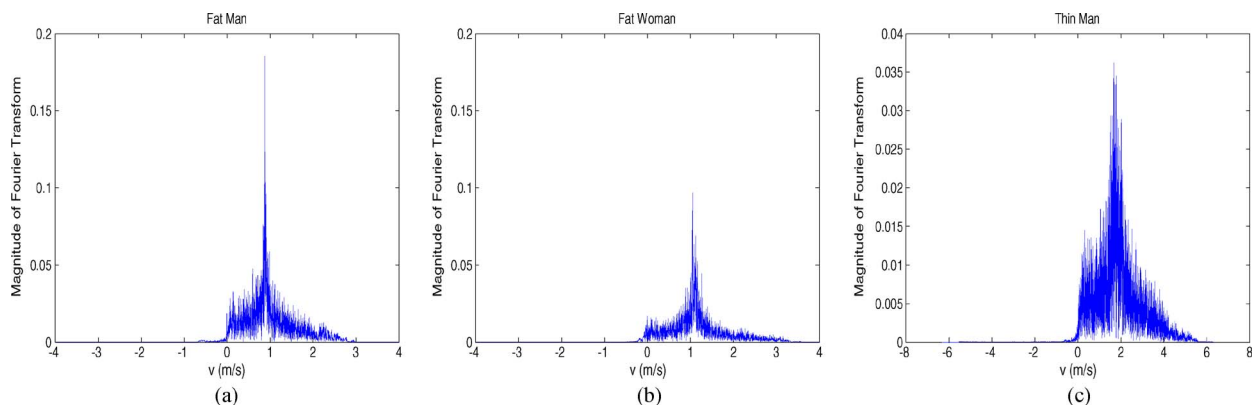

Fig. 11. Doppler spectra of walking bodies with different sizes and genders. (a) Oversize male body. (b) Oversize female body. (c) Thin male body.

Once the surface current distribution for all 7500 frames are calculated, the scattered far field can be computed using (12) and (13)—Appendix and the scattering amplitude from (14)—Appendix. Performing Fourier transform on the calculated scattering amplitude yields the Doppler spectrum of the walking human. The Doppler spectrum of a human walking versus frequency and velocity $(\omega/(2k_0))$ is shown in Fig. 9. As can be observed, the spectrum contains a wide range of velocity values from −1 m/s to over +5.4 m/s. The negative velocities come from the backward motion of legs and arms which is partly compensated with the average positive velocity. The spectrum is maximum around the average velocity of +1.8 m/s. The power density around the average velocity (mean Doppler shift) is dominated by the torso return. The maximum velocity found here is about +5.4 m/s. Therefore, the accuracy of the assumed maximum velocity and the resulting sampling rate is confirmed. We have also simulated different parts of the body separately in order to isolate and study the individual responses.

The body is separated into six parts including the torso, the head, the left and right legs and arms. The simulation results are presented in Fig. 10. Investigating the spectra, we can realize that the spectra of the head and torso are very similar since the way these components move are alike except for the fact that the torso response has higher level given its larger cross section. The spectra extend from +1.5 to +2.1 m/s, around the average velocity. To simulate these parts separately, v_{max} is chosen to be +2.1 m/s. This implies that fewer frames are required and processing time is shorter. On the other hand, the limbs contain higher frequency content and hence higher velocity values, as expected from their movement. The hands' and arms' spectra extend from −1 to +4 m/s with lower levels while the spectra of the legs extend from 0 to 5.4 m/s with higher backscatter levels. It can be inferred from the results that the fastest motion occurs at the feet.

The total spectrum of walking human body is a combination of the spectra of individual parts. As we are concerned about

concealed carried objects on the torso, our next goal is to extract the spectrum of the torso out of the overall radar response. Since all spectra are overlapping and have nonzero values between $+1.5$ to $+2.1$ m/s, we cannot isolate the spectrum of the torso by simple filtering. One can attempt to use simple models to create a matched filter for the moving parts, but due to the complex shape and motion of the body parts and their motions, such matched filters are incapable of separating the desired radar responses. In Section V, this problem is addressed by making use of time-frequency analysis and temporal variations of the scattering amplitude and polarization signature.

B. Effect of Body Size and Gender on the Doppler Spectrum

It is also interesting to investigate how variations in body size and gender affect the Doppler spectrum and whether the measured backscatter Doppler spectrum can be used to distinguish such variations. To study such effects, three other human bodies which are shown in Fig. 4 are simulated. These together with the thin female body considered before constitute the extreme cases for male and female subjects. To consider extreme cases of motion, the large size human models are designed to be walking more slowly with limited motions in the limbs whereas the thin bodies are made to be faster with higher dynamics of movement.

The scattering model is run for these human models as before for a two-step motion to capture their Doppler spectra and the results are presented in Fig. 11. The distinguishing features that separate the female and male bodies can also be recognized by the level of RCS which is higher for the male subjects due to the larger size. The maximum, minimum, and average velocities of the thin male body are similar to those of the thin female body, while the RCS level is higher. Doppler spectra with narrow bandwidth and the energy concentrated mostly around the average velocity belong to oversize and slow bodies whereas a wideband spectrum in which energy is more uniformly distributed in the band belongs to a thin and dynamic person.

Also, a scenario in which the direction of motion and radar to target line of sight are not parallel is considered. The Doppler spectrum of the thin woman who is moving in a direction $45°$ with respect to the radar line of sight is presented in Fig. 12. As observed, the spectrum is compressed as the radial velocities of different body components are reduced. Despite the fact that the Doppler bandwidth is smaller at oblique incidence, it is still possible to distinguish the thin bodies from the bigger and slower bodies at normal incidence, since the backscatter energy is distributed within the band unlike the spectrum of oversize bodies.

C. Dog

The same procedure is performed for a walking dog to evaluate the Doppler spectrum. The electric permittivity of the skin is approximated to be similar to that of humans, while the effect of a 1-cm layer of thick hair covering the skin can be modeled as a homogeneous anisotropic medium with the effective permittivity ε_{eff}. This effective permittivity can
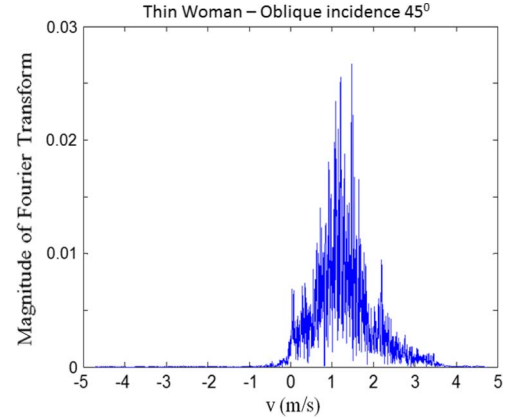

Fig. 12. Doppler spectrum of a thin woman obliquely walking with respect to the radar with $45°$ angle. It is observable that the velocity content is lower, the maximum velocity is 3.8 (which is $5.4/\sqrt{2}$ as expected). However, it is definitely not a oversize body since the energy is not highly concentrated around the average velocity.

be obtained from a dielectric mixing formula for a medium composed of thin vertical cylinders, representing hair stands, in air background. Using the Polder–van Santen Formula [19], the values of ε_{eff} for TE and TM waves are calculated from

$$\text{TM} : \varepsilon_{eff} = \varepsilon_{air} + f(\varepsilon_{hair} - \varepsilon_{air})$$

$$\text{TE} : \varepsilon_{eff} = \varepsilon_{air} + f(\varepsilon_{hair} - \varepsilon_{air}) \frac{2}{\varepsilon_{hair} + \varepsilon_{air}} \quad (4)$$

where f is the volume fraction of hair which is approximately 10%. For this target, the radii of the body's curvature are also much larger than the wavelength at W-band and the PO method is still valid. Hence, an attenuating isotropic layer with the above effective dielectric constant is considered on top of the skin to model the hair layer.

A linear interpolation is used to achieve the required frames for the spectral analysis. Compared to human simulations, a smaller number of frames is needed because the dog is animated to walk slower than the human subject.

For a scenario where the dog is walking toward the radar (front side illumination), Fig. 13 represents the electric current distribution on the dog's face at one specific time step. After evaluating the surface current distribution for all 6000 frames, the far fields are computed from (12), the scattering amplitude from (14) and the Doppler spectrum. Fig. 14 shows the Doppler spectrum of the walking dog versus velocity $(\omega_0/(2k_0))$. As can be seen, the velocities of different body parts spread from -0.2 m/s to 2.5 m/s while the average is around 0.8 m/s. The range of periodic motion for the dog is smaller, as expected.

Comparison of the Doppler spectra of walking human and dog demonstrates the major distinctions in maximum, minimum, and average velocities as well as the spectral levels. The difference between the human and the dog motion and sizes are adequately reflected in their Doppler spectra, giving rise to a measure for distinguishing between these targets. It is observable that the backscatter Doppler spectra of human subjects (different size and gender) and quadrupeds are sufficiently different from each other that can be used as a distinguishing measure.
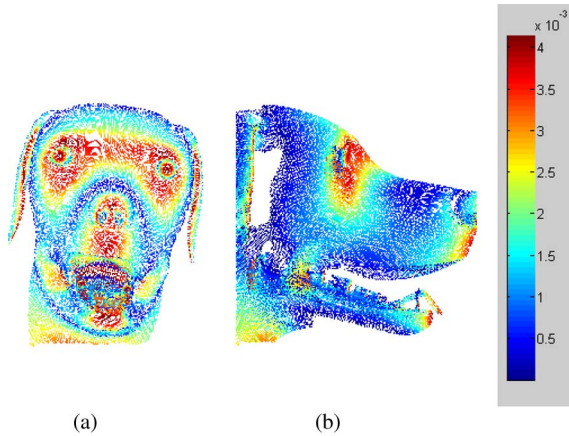
Fig. 13. PO current distribution at 95 GHz on the surface of the dog's face with the incident field 1 V/m. (a) Front view. (b) Side view.
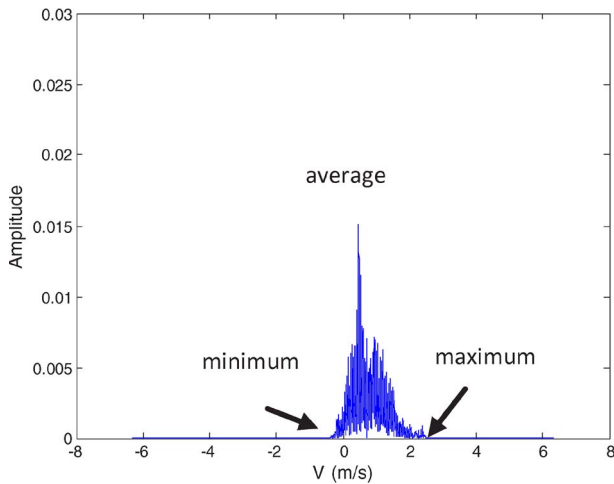

Fig. 14. Doppler spectrum of the co-pol radar response of the dog versus velocity $\omega_0/(2k_0)$. The magnitude is lower than that of human's since the cross section is smaller. Also, the bandwidth is narrower since the range of dog's motion is smaller than that of human's.

V. RADAR BACK SCATTER DECOMPOSITION

The Doppler spectrum was shown to be a relatively good discriminator to distinguish different moving targets. A more challenging question is whether the backscatter data can be used for detecting concealed objects carried by individuals. For this, the Doppler spectrum of the object may not be sufficient by itself. Here, we explore the feasibility of detecting body-attached irregular objects by decomposing the overall backscatter response in terms of its origin from different body parts. The shapes of most concealed objects, unlike the human body, are not smooth or symmetric and as a result can produce significant cross-polarized response. However, when the body is moving, cross-polarized backscatter is increased since concave surfaces are formed and the interactions between different body components are increased. Considering the fact that concealed objects are commonly carried around the torso, and that the torso is primarily convex and on its own does not generate significant cross-polarized backscatter response, the cross-polarized response generated by a concealed object and its interaction with the torso can increase the cross-polarized

response of the torso in the presence of the concealed object. This indicates that if the polarimetric backscatter response of the torso can be isolated, then one can detect the presence of a concealed irregular object attached to the torso. To examine this hypothesis, the polarimetric backscatter from the torso alone is computed. Since the aspect angle can change during walking the polarimetric response over a range of incidence angles must be examined. This can be done by averaging, but we need to ensure that the polarimetric response is preserved. This can be done through the use of the Mueller matrix given by [15]

$$M = [R^T]^{-1} W R^{-1} \tag{5}$$

where

$$R = \begin{bmatrix} 1 & 1 & 0 & 0 \\ 1 & -1 & 0 & 0 \\ 0 & 0 & 1 & 1 \\ 0 & 0 & -j & j \end{bmatrix}$$

$$W = \begin{bmatrix} S_{vv}S_{vv}^* & S_{vh}S_{vh}^* & S_{vh}S_{vv}^* & S_{vv}S_{vh}^* \\ S_{hv}S_{vh}^* & S_{hh}S_{hh}^* & S_{hh}S_{hv}^* & S_{hv}S_{hh}^* \\ S_{hv}S_{vv}^* & S_{hh}S_{vh}^* & S_{hh}S_{vv}^* & S_{hv}S_{vh}^* \\ S_{vv}S_{hv}^* & S_{vh}S_{hh}^* & S_{vh}S_{hv}^* & S_{vv}S_{hh}^* \end{bmatrix} \tag{6}$$

where S_{ij} is the scattering parameter when the incident wave is in the j-polarized and the scattered field is measured in the i-polarization. The elements of the Mueller matrix can be averaged over the desired angles of illumination. The response of the torso for any arbitrary combination of transmit and receive polarizations can be calculated from

$$P(\chi, \psi) = SMS^T \tag{7}$$

where

$$S = \begin{bmatrix} 1 & \cos(2\psi)\cos(2\chi) & \sin(2\psi)\cos(2\chi) & \sin(2\chi) \end{bmatrix}. \tag{8}$$

Here, ψ and χ are the orientation (-90 to $+90$) and the ellipticity angles, respectively (-45 to $+45$). The polarization response of the torso is represented in Fig. 15 and is compared with that of a metallic sphere. It is observable that the copolarized response is maximum for linear and minimum for the circular polarizations, which is similar to that of a sphere indicating the dominance of single-bounce backscatter component.

In the presence of an external irregular object, the polarimetric backscatter will undergo a change that can be used for detection. The change in the polarimetric backscatter from the torso and an external object is due to the direct backscatter of the object and its interaction with the torso (shadowing and multiple scattering). Hence, by isolating the polarimetric response of the torso, it is possible to detect the existence of concealed irregular objects.

We have explored an approach to extract the response of the torso based on the temporal deviations in the RCS response for the body during walking and the time-frequency analysis. In this approach, complex time varying responses from the limbs are removed from the overall backscatter to isolate the response of the torso.
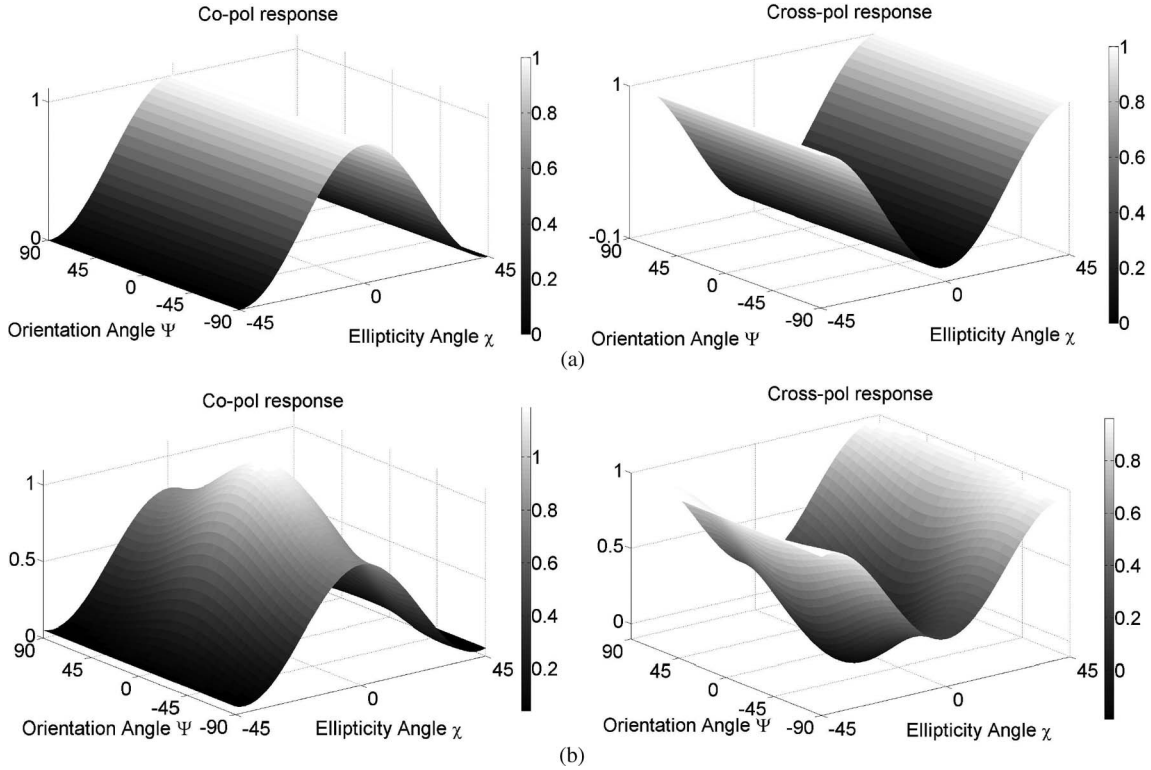
Fig. 15.   (a) Polarization response of sphere and (b) torso.

A. Temporal Variation of Body RCS

To isolate the response of the torso from the full body, we can take advantage of the variations in the response of legs and arms during walking. While the torso response is nearly constant at different instances of walking, the responses of the limbs undergo a major change due to considerable differences in their orientation and position with respect to the radar. At instances when the limbs are spread out, a lower backscattering response from the limbs is expected since their projected cross section in the beam is smaller and, more importantly, the specular reflection from most facets are away from the backscatter direction. On the other hand, when the limbs are aligned with the body, their physical cross section is higher, and there are many facets with their specular reflection in the backscatter direction. Fig. 16 shows the backscattering response of limbs at different instances of walking positions. As predicted, it is observed that the limbs backscatter is lower at the moments when the limbs are spread out (when the axial orientation is such that the specular component of the scattered field is away from the backscattering direction) and is higher when they are aligned with the body. Fig. 17 represents the walking body at different positions. It is shown that at $t = 0.15$ s and $t = 0.65$ s, the limbs are spread out, and their RCS is lower as shown by Fig. 16. Similarly, around $t = 0.4$ s and $t = 0.9$ s, the limbs are aligned with the body and their backscatter response is higher.

It is also interesting to compare the backscatter responses of the torso and limbs at different walking positions. Table II presents the RCS of the torso, RCS of limbs and their ratio at the same walking positions shown in Fig. 17. It shows that the
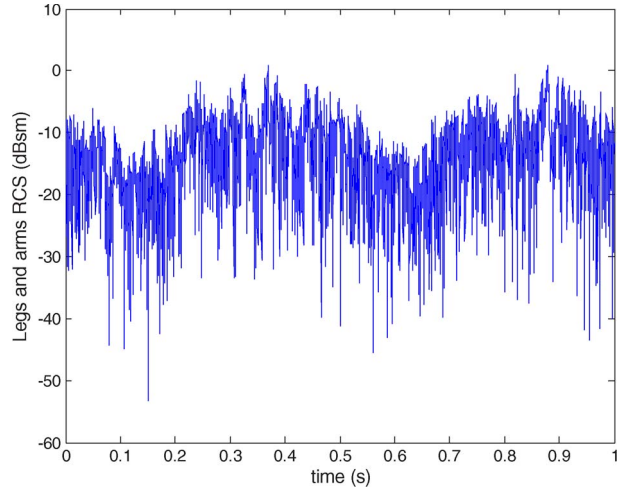

Fig. 16.   Backscattering response of the legs and arms during walking for different walking positions. It is lower when they are spread out ($t = 0.15$ s, $t = 0.65$ s) and higher when they are aligned with the body ($t = 0.4$ s, $t = 0.9$ s).

responses of the limbs are lower at $t = 0.15$ s and $t = 0.65$ s; therefore, the ratio of the torso response to the limbs' response is high. Similarly, at $t = 0.4$ s and $t = 0.9$ s, the response of legs and arms are significantly higher, so that the ratio of the response of the torso to the limbs is much lower. The amount of difference in RCS represents a sufficient contrast in motion detection.

The response of the torso does not undergo a significant change during walking due to its minimal motion during walking. This feature can be utilized to isolate the response of limbs

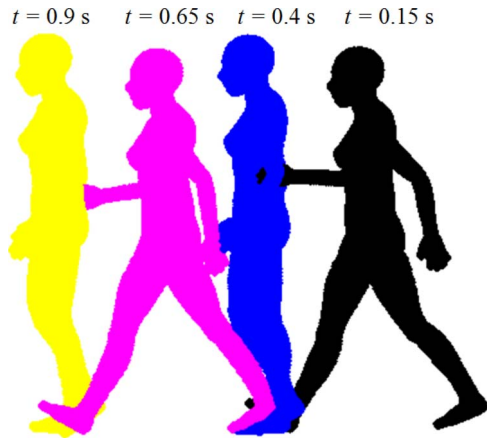$t = 0.9$ s $t = 0.65$ s $t = 0.4$ s $t = 0.15$ s

Fig. 17. Position of human body during walking at different time frames (approaching the radar). It is observable that around $t = 0.15$ s and $t = 0.65$ s where the legs and arms are spread out, the RCS of legs and arms are lower as shown by Fig. 16. Similarly, around $t = 0.4$ s and $t = 0.9$ s, when the legs and arms are aligned with the body, the response is higher.

TABLE II
RCS OF THE TORSO AND LEGS AND ARMS AND ALSO, THEIR RATIO AT FOUR SAMPLE POSITIONS WHERE THE LEGS AND ARMS EITHER ALIGNED WITH TORSO OR ARE SPREAD OUT

	Torso RCS (dBsm)	Limbs RCS (dBsm)	Ratio
$t = 0.15$ s	-6.0208	-18.4051	+12.3843
$t = 0.4$ s	-7.075	+3.964	-11.0387
$t = 0.65$ s	-4.5727	-11.6678	+7.0951
$t = 0.9$ s	-7.2096	+4.1284	-11.3379

from the rest of the body. The response of the body at the moments when the cross section of legs and arms are small can be mainly attributed to the torso. For example, the response of the body between 0.1 s ∼ 0.2 s and 0.6 s ∼ 0.7 s (almost 20% of the walking time) can be considered the contribution of the torso to a large extent.

B. Time-Frequency Analysis

During walking, there are moments at which limbs' velocities have the most difference with the velocity of the torso. This of course can also be observed in the radar backscatter Doppler spectra if time-frequency analysis is used [18]. To capture the temporal spectra, the time domain backscatter signal is divided into a number of subsignals over an appropriate time interval. Each of these signals represents a time frame (with 0.01 s length) during walking. The Fourier transformation is then performed on these subsignals, yielding a set of spectra in discrete time steps. To avoid spurious response in the frequency domain, the backscatter signal in time domain is multiplied by a series of shifted overlapping Gaussian signals. These signals are Fourier transformed, and the result is shown in the 2-D plots of Fig. 18(a) for the thin female model. The observed time domain spectra of backscatter signal reveals detailed features of walking positions. If the selected frames happen to be at the moment where the limbs have their maximum velocities (limbs aligned with the torso), the spectrum is wide and centered around the average velocity for the torso (+1.8 m/s). At another

instance, when the legs and arms velocities are minimum, the spectrum is narrower. In this situation, as presented in the previous section, the response of the limbs is about 20 dB lower. In Fig. 18(b) and (c), the time-frequency responses of the limbs and torso individually are presented. It is shown that around $t = 0.15$ s and $t = 0.65$ s, the bandwidth of the limbs spectrum is narrow, has lower level, and is centered around the torso's average velocity. On the other hand, when limbs have their maximum velocities, their spectrum is wideband. In this case, the total backscatter power is higher, but spread out in the spectrum. Hence, there seem to be two approaches to isolate the response of the torso, one is to identify the frame where bandwidth is minimum, and the other one is to identify the frame where the bandwidth is maximum and filter out the high- and low-frequency components. Fig. 19 shows two temporal backscatter responses: 1) the response of the body when the spectrum is narrow (around $t = 0.15$ s), and 2) the response of the body when the spectrum is wideband (around $t = 0.4$ s). A Gaussian bandpass filter centered at 1140 Hz (corresponding to 1.8 m/s), and 3-dB band width of 210 Hz is used to isolate the response of the torso. The filtered responses of the frames closely resemble that of the torso alone at both instances. This method can be used to isolate the response of the torso from the rest of the body for detecting concealed objects around the torso as presented in the next section. It should also be noted that the small differences in the response of the torso in Fig. 19(a) and (b) are due to the fact that the posture of the torso itself varies a small amount during walking and the Doppler spectrum has a bandwidth as previously shown in Fig. 10.

C. Polarimetric Time-Frequency Analysis for Detection of Concealed Objects

As mentioned before, the backscatter response of the torso does not generate any substantial amount of cross-polarized backscatter. On the other hand, the irregular shape of most concealed objects, such as handguns and firearms, can produce a noticeable amount of cross-polarized backscatter response. Also, when an object is carried on or around the torso, the interaction between the torso and the object can generate cross-polarized response as well. This feature can be exploited to detect concealed objects. The procedure for isolating the torso response from the limbs was described in the previous section. We can apply this technique to the fully polarimetric backscatter response and isolate the polarimetric response of the torso from the total backscatter response and hence improving the probability of detection and reducing the false alarm at the same time. The polarimetric analysis is based on examining the ratio of cross-polarized/copolarized response to explore the presence of objects. To examine the performance of this approach, the polarimetric scattering simulation of a walking human carrying a handgun is studied.

To begin with, the gun model is incorporated over the human model mesh as shown in Fig. 20. The gun is moved with the moving body by having it anchored to one of the facets of the waist. Since the handgun is made of metal, the perfect electric conductor boundary condition is used.
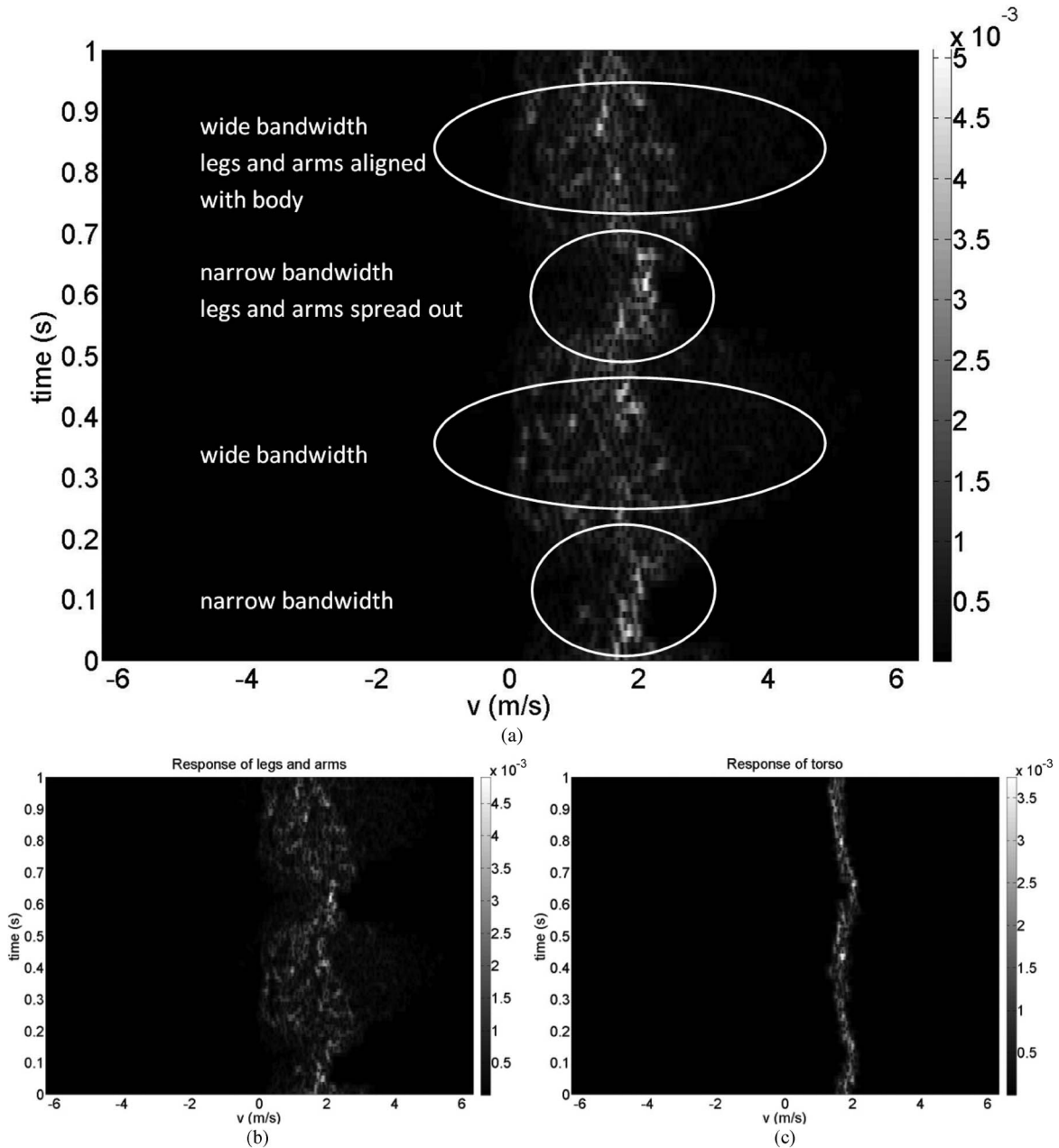
Fig. 18. Co-polarized response of the human body is Fourier transformed using time-frequency analysis. (a) Full body, (b) the limbs, and (c) the torso. The signal is chopped into a number of sub-signals using a number of shifted Gaussian signals and the Fourier transformed is performed on the resulting sub-signals. The plots show different bandwidths for different frames. For the full body, while there are moments (around $t = 0.4$ s and $t = 0.9$ s) in which the velocity of the legs and arms are maximum and bandwidth is wide, there are some other times (around $t = 0.15$ s and $t = 0.65$ s) that their velocity is minimum and the bandwidth is narrow. The bandwidth of the limbs' spectrum is narrow around $t = 0.15$ s and $t = 0.65$ s and confined around the same velocity as torso is located. At other moments, when legs and arms have higher velocities, their spectrum is wideband and spread out, while the spectrum of torso is narrow around the middle velocity at all times.

The IPO model is used to analyze the polarimetric response of the handgun and human body including all interactions up to the third order in the vicinity of the gun. The time-frequency analysis is applied to both co- and cross-polarized responses to isolate the response of the torso. For this purpose, from the time-frequency signal, the instances with maximum and minimum bandwidths are found. Then, the signal is filtered around the average velocity of the body in order to isolate the response of the torso. The ratios of cross- to copolarized responses of the isolated torso obtained from the filtering

approach for both cases of with and without the handgun are calculated. Table III shows the results for these cases, one where the spectrum is narrow and the other where the spectrum is wide. It is shown that the ratio is increased up to about 7 dB and 3.5 dB, respectively, using the filtering approach. To demonstrate the overall improvement achieved, the ratio of the cross- to copolarized backscatter ratios in the presence and absence of the handgun without applying time-frequency analysis, is also calculated and included in Table III. As shown in the table, the cross- to copolarized response of the entire
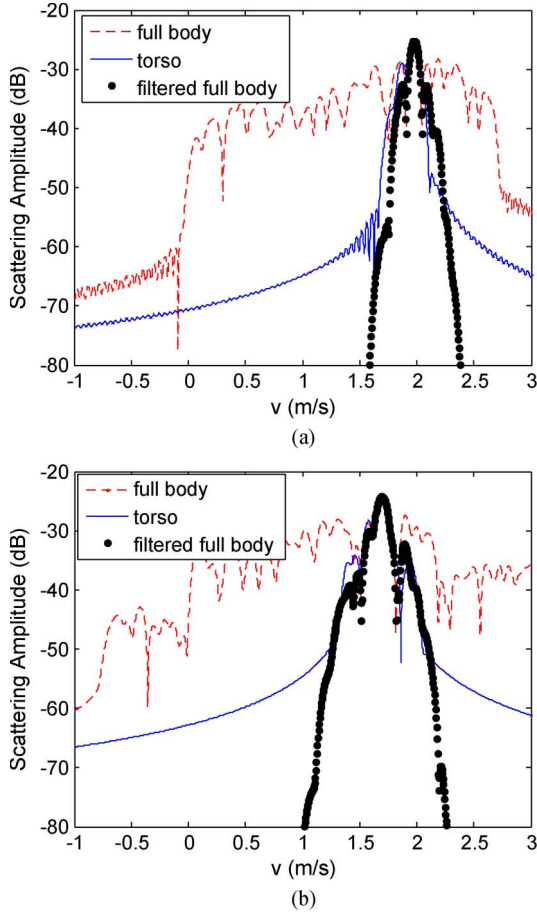
Fig. 19. Temporal backscattering response of torso and the full body at two instances. (a) The limbs are spread out and the spectrum is narrow. (b) The limbs are aligned with the body and the spectrum is wide. The filtered response of the full body resembles that of the torso alone at both instances.
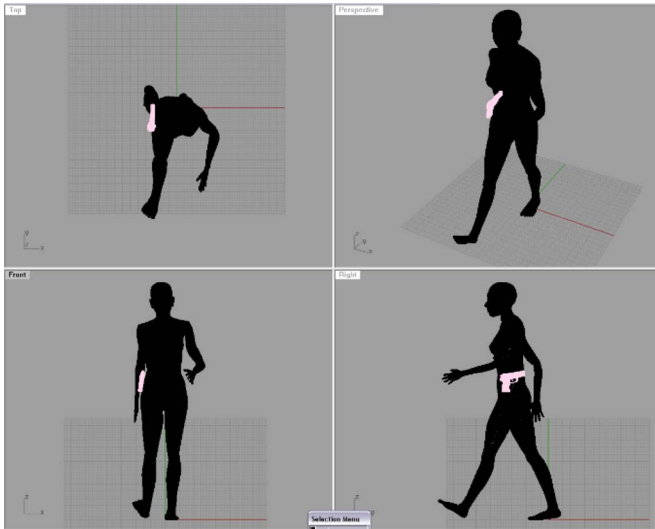

Fig. 20. Gun is placed on the human waist where a handgun is actually carried.

body is only 0.5 dB higher when the handgun is present which is not high enough to be used as a means of detection. This highlights the fact that the combination of radar polarimetry in

TABLE III
CROSS- TO COPOLARIZED RESPONSE OF A WALKING HUMAN BODY AT TWO INSTANCES, WHERE THE LIMBS ARE ALIGNED WITH THE BODY AND WHERE THEY ARE SPREAD OUT. THE RESPONSE IS INCREASED WHEN THE HANDGUN IS PRESENT

cross- to co-polarized response	Without hand gun (dB)	With handgun (dB)	Ratio (dB)
spread-out position (narrow bandwidth, t = 0.15)	-15.4	-8.23	+7.17
aligned position (wide bandwidth t = 0.4 s	-21.1	-17.58	+3.52
the entire body without using time-frequency analysis	-18.6	-18.11	+0.5

conjunction with the time-frequency analysis can lead to the detection of metallic objects at a standoff location without the need for high resolution imaging which is the common practice. It should also be noted that since a Doppler filter is applied to the backscatter data, all stationary objects that can produce cross-polarized response are also filtered out. This adds to the robustness of the algorithm and can drastically reduce the false alarm rate.

VI. CONCLUSION

In this paper, the Doppler spectra of MMW backscatter response of different walking human bodies and dog are investigated. It is shown that the Doppler spectra are different both in amplitude and bandwidth which allows one to distinguish between different targets and characterize size, gender, and posture to some extent. In addition, the motion of different body components such as the torso, head, legs, and arms produce Doppler spectra. Furthermore, radar polarimetry is used as a tool for detection of concealed objects on human body. It is shown that irregular objects increase the level of cross-polarized backscatter. However, to be able to detect this change easily, time-frequency analysis is applied to dissect the overall backscatter response into the corresponding backscatter responses of different body parts. Utilizing this method, we demonstrated markedly enhanced detection. This approach allows standoff detection of concealed objects on human body.

APPENDIX

PO/IPO Model

The scattered field from a dielectric object can be computed from a set of fictitious surface currents which are directly related to the tangential field components and are given by

$$\vec{J}_s(\vec{r}) = \hat{n} \times \vec{H}_i(\vec{r}) + \hat{n} \times \vec{H}_s(\vec{r})$$

$$\vec{M}_s(\vec{r}) = -\hat{n} \times \vec{E}_i(\vec{r}) - \hat{n} \times \vec{E}_s(\vec{r}). \tag{9}$$

Here, $\vec{J}_s$ and $\vec{M}_s$ are the induced surface currents, $\vec{H}_i, \vec{E}_i$ are the magnetic and electric incident fields, and $\vec{H}_s, \vec{E}_s$ are the magnetic and electric scattered fields. Here, $\vec{H}_i, \vec{E}_i$ are plane waves, i.e., $\vec{H}_i(\vec{r}) = \vec{H}_0 e^{jk_0 \hat{k}_i \cdot \vec{r}}$, $\vec{E}_i(\vec{r}) = \vec{E}_0 e^{jk_0 \hat{k}_i \cdot \vec{r}}$. In the PO approach, the scattered fields are approximated by

the reflected fields from a local tangent plane (representing the interface of a half-space dielectric medium). The target surface is discretized into nonuniform small facets and by defining $\hat{t} = \hat{k}_i \times \hat{n}/|\hat{k}_i \times \hat{n}|$, the incident and reflected fields over each facet is decomposed into parallel and perpendicular components, i.e.,

$$\vec{E}_i(\vec{r}) = \left(A(\hat{k}_i \times \hat{t}) + B\hat{t} \right) e^{jk_0\hat{k}_i \cdot \vec{r}}$$

$$\vec{H}_i(\vec{r}) = \frac{1}{Z_0} \left(B(\hat{k}_i \times \hat{t}) - A\hat{t} \right) e^{jk_0\hat{k}_i \cdot \vec{r}}$$

$$\vec{E}_r(\vec{r}) = \left(AR_{TM}(\hat{k}_r \times \hat{t}) + BR_{TE}\hat{t} \right) e^{jk_0\hat{k}_i \cdot \vec{r}}$$

$$\vec{H}_r(\vec{r}) = \frac{1}{Z_0} \left(BR_{TE}(\hat{k}_r \times \hat{t}) - AR_{TM}\hat{t} \right) e^{jk_0\hat{k}_i \cdot \vec{r}} \quad (10)$$

where $A = -Z_0\vec{H}_0 \cdot \hat{t}$, $B = \vec{E}_0 \cdot \hat{t}$, Z_0 is the characteristic impedance of free space (377 Ω), and R_{TE} and R_{TM} are the Fresnel reflection coefficients for TE and TM polarizations, respectively. After some algebraic manipulation, the induced surface currents are [15]

$$\vec{J}_s(\vec{r}) = e^{jk_0(\hat{k}_i \cdot \vec{r}')} \left[\frac{1}{Z_0}(\vec{E}_0 \cdot \hat{t})(\hat{n} \cdot \vec{k}_i)(1 - R_{TE})\hat{t} \right.$$
$$\left. + (\vec{H}_0 \cdot \hat{t})(1 + R_{TM})(\hat{n} \times \hat{t}) \right]$$

$$\vec{M}_s(\vec{r}) = - e^{jk_0(\hat{k}_i \cdot \vec{r}')} \left[Z_0(\vec{H}_0 \cdot \hat{t})(\hat{n} \cdot \vec{k}_i)(1 - R_{TM})\hat{t} \right.$$
$$\left. + (\vec{E}_0 \cdot \hat{t})(1 + R_{TE})(\hat{n} \times \hat{t}) \right]. \quad (11)$$

Once the equivalent surface currents are obtained, the far field can be calculated from

$$\vec{E}_s(r) = \frac{jk_0 e^{jk_0 r}}{4\pi r}(\bar{\bar{I}} - \hat{k}_s\hat{k}_s)$$
$$\cdot \iint_S \left[Z_0\vec{J}_s(\vec{r}') - \hat{k}_s \times \vec{M}_s(\vec{r}') \right] e^{-jk_0\hat{k}_s \cdot \vec{r}'} ds' \quad (12)$$

where $\hat{k}_s$ is the direction of observation.

To calculate the electromagnetic interactions among body parts, the second-order surface currents must be calculated. This is done using the exact dyadic Greens function. Considering the interaction of two facets, the field induced on surface 2 due to the first order currents on surface 1 is calculated using [16]

$$\vec{H}_{2,1}^{second}\left(r, \vec{J}_1^{first}(\vec{r}'), M_1^{first}(\vec{r}') \right)$$
$$= \iint_S \vec{J}_1^{first}(\vec{r}') \times \nabla g_0 ds + \frac{1}{jk_0 Z_0}\nabla$$
$$\times \iint_S \vec{M}_1^{first}(\vec{r}') \times \nabla g_0 ds$$

$$\vec{E}_{2,1}^{second}\left(r, \vec{J}_1^{first}(\vec{r}'), M_1^{first}(\vec{r}') \right)$$
$$= - \iint_S \vec{M}_1^{first}(\vec{r}') \times \nabla g_0 ds + \frac{1}{jk_0 Y_0}\nabla$$
$$\times \iint_S \vec{J}_1^{first}(\vec{r}') \times \nabla g_0 ds \quad (13)$$

where $g_0 = e^{jk_0 r}/4\pi r$ is the free space Green's function, Z_0 and Y_0 are the impedance and admittance of free space, and $\vec{r}, \vec{r}'$ are the positions of surfaces 2 and 1, respectively. The second-order currents which are induced on surface 2 are calculated from the tangential components of the second-order fields. The iterative procedure can be continued until the total currents converge. It is shown that due to free space path loss, higher order fields are trivial and currents converge quickly, particularly for the human body, in which the component sizes are much larger than the wavelength.

When the total scattered field of a complex target is calculated, the entries of the scattering matrix (S) can be determined from

$$S_{hh} = \frac{E_s^h r_0 e^{-jk_0\hat{k}_i\vec{r}}}{E_i^h} \quad S_{hv} = \frac{E_s^h r_0 e^{-jk_0\hat{k}_i\vec{r}}}{E_i^v}$$

$$S_{vh} = \frac{E_s^v r_0 e^{-jk_0\hat{k}_i\vec{r}}}{E_i^h} \quad S_{vv} = \frac{E_s^v r_0 e^{-jk_0\hat{k}_i\vec{r}}}{E_i^v} \quad (14)$$

where r_0 is the distance from the target to the observation point.

REFERENCES

[1] R. W. McMillan, N. C. Currie, D. D. Ferris, Jr., and M. C. Wicks, "Concealed weapon detection using microwave and millimeter wave sensors," in *Proc. Microw. Millimeter Wave Technol.*, 1998, pp. 1–4.

[2] V. B. Shteinshleinger, G. A. Koshevarov, L. Y. Melnikov, G. S. Misezhnikov, A. Y. Onin, and V. I. Zagatin, "A new type of device to locate objects hidden under the clothes of people," in *Proc. CIE Int. Conf.*, 2001, pp. 227–230.

[3] F. M. Henderson and Z. Xia, "SAR applications in human settlement detection, population estimation and urban land use pattern analysis: A status report," *IEEE Trans. Geosci. Remote Sens.*, vol. 35, no. 1, pp. 79–83, Jan. 1997.

[4] P. van Dorp and F. C. A. Groen, "Human walking estimation with radar," *Proc. Inst. Elect. Eng.—Radar Sonar Navig.*, vol. 150, no. 5, pp. 356–365, Oct. 2003.

[5] T. Dogaru, C. Le, and G. Kirose, "Time-frequency analysis of a moving human Doppler signature," Army Research Lab., Adelphi, MD, Tech. Rep. ARL-TR-4728, Feb. 2009.

[6] G. E. Smith, K. Woodbridge, and C. J. Baker, "Multistatic micro-Doppler signature of personnel," in *Proc. IEEE Radar Conf.*, 2008, pp. 1–6.

[7] Y. Kim and H. Ling, "Human activity classification based on microDoppler signatures using a support vector machine," *IEEE Trans. Geosci. Remote Sens.*, vol. 47, no. 5, pp. 1328–1337, May 2009.

[8] B. G. Mobasseri and M. Amin, "A time-frequency classifier for human gait recognition," in *Proc. SPIE Defense, Security Sens.*, 2009, vol. 7306, pp. 730 628-1–730 628-9.

[9] C. Hornsteiner and J. Detlefsen, "Characterisation of human gait using a continuous-wave radar at 24 GHz," *Adv. Radio Sci.*, vol. 6, pp. 67–70, May 2008.

[10] D. M. Sheen, D. L. McMakin, and T. E. Hall, "Three-dimensional millimeter-wave imaging for concealed weapon detection," *IEEE Trans. Microw. Theory Technol.*, vol. 49, no. 9, pp. 1581–1592, Sep. 2001.

[11] H. D. Collins, D. L. McMakin, T. E. Hall, and R. P. Gribble, "Real-time holographic surveillance system," U.S. Patent 5 455 590, Oct. 3, 1995.

[12] H. F. Cook, "Dielectric behavior of some types of human tissues at microwave frequencies," *Br. J. Appl. Phys.*, vol. 2, no. 10, pp. 295–300, Oct. 1951.

[13] T. Walters, D. W. Blick, L. R. Johnson, E. R. Adair, and K. R. Foster, "Heating and pain sensation produced in human skin by millimeter waves: Comparison to a simple thermal model," *Health Phys.*, vol. 78, no. 3, pp. 259–267, Mar. 2000.

[14] C. Gabriel and S. Gabriel, "Compilation of the dielectric properties of body tissue at RF and microwave frequencies," Final Report for AFOSR/NL Bolling AFB DC 20332-0001, Jun. 1996.

[15] F. T. Ulaby and C. Elachi, *Radar Polarimetry for Geoscience Applications.* Norwood, MA: Artech House, 1990.

[16] F. Obelleiro, M. G. Araujo, and J. L. Rodriguez, "Iterative physical-optics formulation for analyzing large waveguide with lossy walls," *Microw. Opt. Tech. Lett.*, vol. 28, no. 1, pp. 21–26, Jan. 2001.

[17] M. Dehmollaian and K. Sarabandi, "Electromagnetic scattering from foliage camouflaged complex targets," *IEEE Trans. Geosci. Remote Sens.*, vol. 44, no. 10, pp. 2698–2709, Oct. 2006.

[18] [Online]. Available: http://www.makehuman.org/blog/index.php

[19] D. Polder and J. H. van Santen, "The effective permeability of mixtures of solids," *Physica*, vol. 12, no. 5, pp. 257–271, Aug. 1946.

[20] S. Qian, *Introduction to Time-Frequency and Wavelet Transforms.* Englewood Cliffs, NJ: Prentice-Hall, 2002.

Mehrnoosh Vahidpour (S'99) received the B.Sc. and M.Sc. degrees in electrical engineering from the University of Tehran, Tehran, Iran, in 2002 and 2005, respectively. She is currently working toward the Ph.D. degree at The University of Michigan at Ann Arbor, Ann Arbor.

Her research interest includes radar remote sensing, millimeter-wave radars, and microfabrication of high-frequency devices.

Kamal Sarabandi (S'87–M'90–SM'92–F'00) received the B.S. degree in electrical engineering from the Sharif University of Technology, Tehran, Iran, in 1980, the M.S. degree in electrical engineering, and the M.S. degree in mathematics and the Ph.D. degree in electrical engineering from The University of Michigan at Ann Arbor, Ann Arbor, in 1986 and 1989, respectively.

He is currently the Director of the Radiation Laboratory and the Rufus S. Teesdale Professor of Engineering in the Department of Electrical Engineering and Computer Science, The University of Michigan at Ann Arbor. He has served as the Principal Investigator on many projects sponsored by the National Aeronautics and Space Administration (NASA), Jet Propulsion Laboratory, Army Research Office, Office of Naval Research, Army Research Laboratory (ARL), National Science Foundation, Defense Advanced Research Projects Agency, and a large number of industries. Currently, he is leading the Center for Microelectronics and Sensors funded by the ARL under the Micro-Autonomous Systems and Technology Collaborative Technology Alliance program. He possesses 25 years of experience with wave propagation in random media, communication channel modeling, microwave sensors, and radar systems and leads a large research group including two research scientists, 12 Ph.D. students. He has graduated 37 Ph.D. and supervised numerous postdoctoral students. He has published many book chapters and more than 190 papers in refereed journals on miniaturized and onchip antennas, metamaterials, electromagnetic scattering, wireless channel modeling, random media modeling, microwave measurement techniques, radar calibration, inverse scattering problems, and microwave sensors. He has also had more than 442 papers and invited presentations in many national and international conferences and symposia on similar subjects. His research areas of interest include microwave and millimeter-wave radar remote sensing, metamaterials, electromagnetic wave propagation, and antenna miniaturization.

Dr. Sarabandi served as a member of NASA Advisory Council appointed by the NASA Administrator for two consecutive terms from 2006–2010. He is serving as a Vice President of the IEEE Geoscience and Remote Sensing Society (GRSS) and is a member of the Editorial Board of the PROCEEDINGS OF THE IEEE. He was an Associate Editor of the IEEE TRANSACTIONS ON ANTENNAS AND PROPAGATION and the IEEE SENSORS JOURNAL. He is a member of Commissions F and D of URSI. He was the recipient of the Henry Russel Award from the Regent of The University of Michigan. In 1999, he received a GAAC Distinguished Lecturer Award from the German Federal Ministry for Education, Science, and Technology. He was also a recipient of the 1996 EECS Department Teaching Excellence Award and a 2004 College of Engineering Research Excellence Award. In 2005, he received the IEEE GRSS Distinguished Achievement Award and the University of Michigan Faculty Recognition Award. He also received the best paper Award at the 2006 Army Science Conference. In 2008, he was awarded a Humboldt Research Award from The Alexander von Humboldt Foundation of Germany and received the best paper award at the IEEE Geoscience and Remote Sensing Symposium. He was also awarded the 2010 Distinguished Faculty Achievement Award from the University of Michigan. The IEEE Board of Directors announced him as the recipient of the 2011 IEEE Judith A. Resnik medal. In the past several years, joint papers presented by his students at a number of international symposia (IEEE APS'95,'97,'00,'01,'03,'05,'06,'07; IEEE IGARSS'99,'02,'07;'11 IEEE IMS'01, USNC URSI'04,'05,'06,'10,'11 AMTA '06, URSI GA 2008) have received best paper awards.